RESEARCH ARTICLE

National Science Review
10: nwac154, 2023
https://doi.org/10.1093/nsr/nwac154
Advance access publication 4 August 2022

PHYSICS

All-electrical switching of a topological non-collinear antiferromagnet at room temperature

Yongcheng Deng[1,2,†], Xionghua Liu[1,2,†], Yiyuan Chen[3,4,†], Zongzheng Du[3,4,†], Nai Jiang[1,2], Chao Shen[1,2], Enze Zhang[1,2], Houzhi Zheng[1,2], Hai-Zhou Lu[3,4,*] and Kaiyou Wang[1,2,5,6,*]

[1]State Key Laboratory for Superlattices and Microstructures, Institute of Semiconductors, Chinese Academy of Sciences, Beijing 100083, China; [2]Center of Materials Science and Optoelectronics Engineering, University of Chinese Academy of Sciences, Beijing 100049, China; [3]Institute for Quantum Science and Engineering and Department of Physics, Southern University of Science and Technology (SUSTech), Shenzhen 518055, China; [4]International Quantum Academy, Shenzhen 518048, China; [5]Beijing Academy of Quantum Information Sciences, Beijing 100193, China and [6]Center for Excellence in Topological Quantum Computation, University of Chinese Academy of Sciences, Beijing 100049, China

***Corresponding authors.** E-mails: luhz@sustech.edu.cn; kywang@semi.ac.cn
[†]Equally contributed to this work.

Received 15 July 2022; **Accepted** 31 July 2022

ABSTRACT

Non-collinear antiferromagnetic Weyl semimetals, combining the advantages of a zero stray field and ultrafast spin dynamics, as well as a large anomalous Hall effect and the chiral anomaly of Weyl fermions, have attracted extensive interest. However, the all-electrical control of such systems at room temperature, a crucial step toward practical application, has not been reported. Here, using a small writing current density of around 5×10^6 A·cm^{-2}, we realize the all-electrical current-induced deterministic switching of the non-collinear antiferromagnet Mn_3Sn, with a strong readout signal at room temperature in the $Si/SiO_2/Mn_3Sn/AlO_x$ structure, and without external magnetic field or injected spin current. Our simulations reveal that the switching originates from the current-induced intrinsic non-collinear spin-orbit torques in Mn_3Sn itself. Our findings pave the way for the development of topological antiferromagnetic spintronics.

Keywords: spintronics, non-collinear antiferromagnetic Weyl semimetals, all-electrical switching, spin-orbit torques

INTRODUCTION

Antiferromagnets have recently attracted tremendous interest as candidates for next-generation spintronics devices, as they have the prospect of offering higher storage density and faster data processing than their ferromagnetic counterparts [1,2]. However, the weak readout signals of conventional collinear antiferromagnets driven by electrical approaches greatly restrict their practical applications [3,4]. Alternatively, large magnetotransport signatures, such as the intrinsic anomalous Hall effect in topological antiferromagnets, could provide a solution to this issue [5,6]. In particular, the non-collinear antiferromagnetic Weyl semimetal Mn_3Sn has recently fascinated the condensed matter physics and information technology communities because of its non-trivial band topology [7,8] and unusual magnetic responses [9–11].

Mn_3Sn hosts an ABAB stacking sequence of the (0001) kagome lattice of Mn (Fig. 1a), with a 120° non-collinear antiferromagnetic ordering of the Mn magnetic moments below the Néel temperature of $T_N \approx 430$ K [9]. This antiferromagnetic state on the kagome bilayers can be viewed as a ferroic ordering of a cluster magnetic octupole (Fig. 1b), which macroscopically breaks the time-reversal symmetry and results in a large anomalous Hall effect [9,12]. With the assistance of an auxiliary magnetic field, the deterministic switching of the magnetic octupole in Mn_3Sn has been achieved by spin-orbit torques from a heavy-metal layer [13,14]. However, as a critical step toward practical application, the field-free manipulation of Mn_3Sn, driven by electrical currents at room temperature, has not been reported. Here, we demonstrate the all-electrical switching of topological antiferromagnetic states in heavy-metal-layer-free Mn_3Sn devices.

RESULTS

Experiments were performed on sputter-deposited Mn_3Sn (50 nm)/AlO_x (2 nm) thin films, and on the reference samples with heavy metals consisting of Ru (3 nm)/Mn_3Sn (50 nm)/AlO_x (2 nm) and Ru

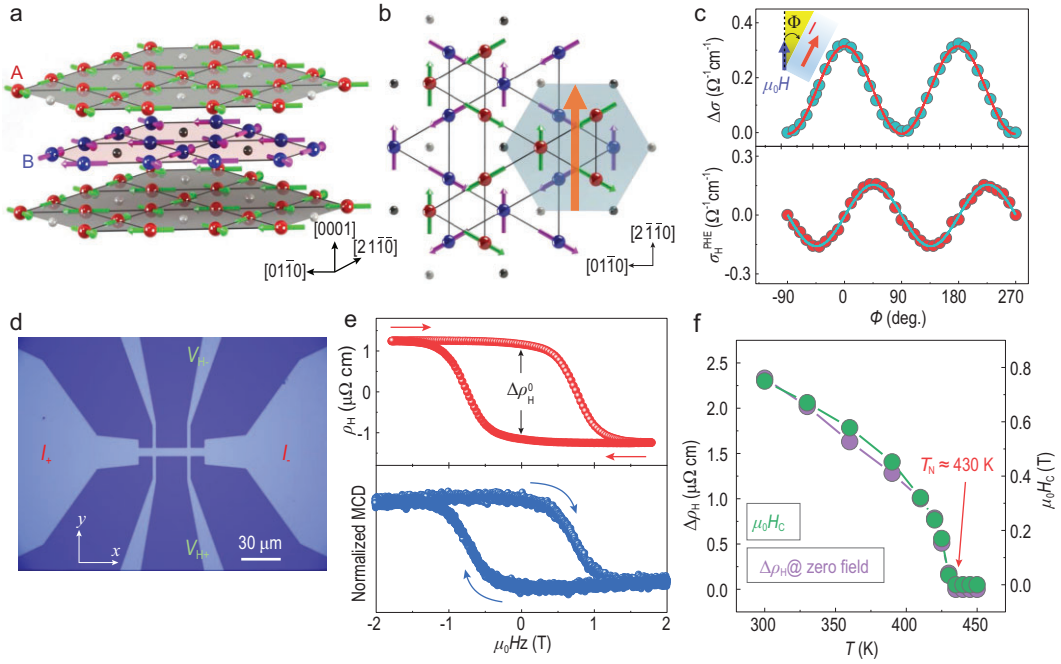

Figure 1. Crystal and magnetic structures, and the magnetotransport and magnetic properties of the Mn_3Sn device. (a) Mn_3Sn crystal structure. The large red and blue spheres (small gray and black spheres) represent the Mn (Sn) atoms at the $z = 0$ and 1/2 planes, respectively. (b) Magnetic structure of Mn_3Sn. The magnetic moments of Mn (green and pink arrows in different layers) are arranged along the kagome planes and form a spin structure with inverse triangular texture. The six adjacent moments between layers (light blue hexagon) constitute ferroic ordering of a cluster magnetic octupole (large orange arrow). (c) Angular dependence of the in-plane longitudinal magnetoconductivity $\Delta\sigma$ (top) and planar Hall conductivity σ_H^{PHE} (bottom) of the 50-nm-thick Mn_3Sn device at room temperature and 1.8 T. The red and cyan solid lines for $\Delta\sigma$ and σ_H^{PHE} are the fitting results using the theoretical equations for the chiral anomaly (Equations S6 and S7 in Supplementary Section S6). (d) Optical micrograph of our fabricated Hall device and measurement scheme. (e) Anomalous Hall resistivity (top) and magnetic circular dichroism (MCD) signal (bottom) versus $\mu_0 H_Z$ for the 50-nm-thick Mn_3Sn device at room temperature. Both of them exhibit clear hysteresis loops with a coercive field $\mu_0 H_C$ of ~0.75 T. (f) Temperature dependence of $\Delta\rho_H^0$ and $\mu_0 H_C$ derived from the hysteresis loops of the 50-nm-thick Mn_3Sn device, suggesting a Néel temperature $T_N \approx 430$ K (Supplementary Fig. S7).

(3 nm)/Mn_3Sn (50 nm)/Pt (8 nm)/AlO_x (2 nm). All samples were deposited on thermally oxidized Si substrate. Unless otherwise stated, all the measurements were performed on the Mn_3Sn (50 nm)/AlO_x (2 nm) materials or devices without heavy metals. We first characterize the structure, transport properties and magnetic properties of Mn_3Sn. The X-ray diffraction peaks of (010) and (020) at 18° and 36° confirm the hexagonal $D0_{19}$ Mn_3Sn structure, and no additional peaks coming from plausible impurity phases were observed [15,16] (see the details in Supplementary Section S1 and more related analysis in Supplementary Sections S2–S4). The microstructure of our film and the chemical composition of $Mn_{3.06}Sn_{0.94}$ were measured by cross-sectional high-resolution transmission electron microscopy (HR-TEM) and energy-dispersive X-ray spectroscopy (EDX) [17,18] (Supplementary Fig. S3), respectively. The magnetotransport phenomena observed in our thin films (Fig. 1c and Supplementary Fig. S4) are consistent with previous measurements [13], where the angular dependence of the in-plane longitudinal magnetoconductivity ($\Delta\sigma = \sigma - \sigma_\perp$) and planar Hall conductivity σ_H^{PHE} can be well fitted by the theoretical equations for the chiral anomaly of Weyl fermions [19] (Fig. 1c and Supplementary Section S6).

We measured the anomalous Hall resistivity ρ_H as a function of the out-of-plane magnetic field $\mu_0 H_Z$ to quantitatively estimate the population of switchable domains in the device (Fig. 1d). A clear hysteresis of the anomalous Hall resistivity with a zero-field change $\Delta\rho_H^0$ is observed (Fig. 1e (top)), which shows that the negative (positive) value of ρ_H is produced by the '$+z$ ($-z$) domain' with the positive $+z$ (negative $-z$) component of the polarization direction of the magnetic octupole [13,15,20,21]. The field-swept measurements of the magnetic circular dichroism (MCD) exhibit a hysteresis loop of $M - \mu_0 H_Z$ with a coercive field of $\mu_0 H_C \approx 0.75$ T (Fig. 1e (bottom)), which is in agreement with the measured anomalous Hall

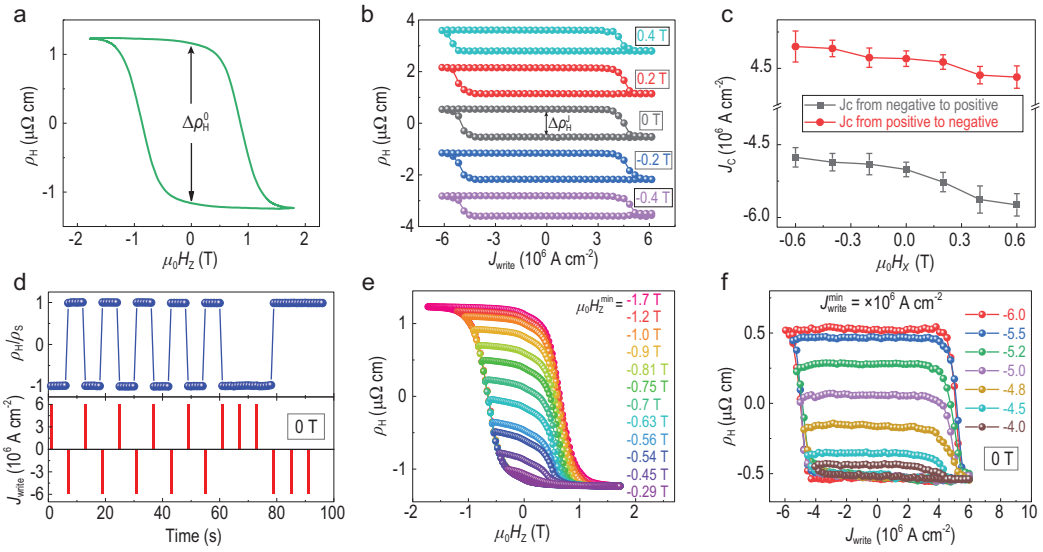

Figure 2. Zero-field current-induced switching of the antiferromagnetic states in the Mn_3Sn device. (a) Anomalous Hall resistivity ρ_H dependence on $\mu_0 H_Z$ for the Mn_3Sn device at room temperature. (b) ρ_H versus J_{write} at $\mu_0 H_x = 0, \pm 0.2$ T, ± 0.4 T for the Mn_3Sn device at room temperature. (c) The critical current density J_c as a function of $\mu_0 H_x$ for positive and negative current-sweeping directions, respectively, of the ρ_H vs. J_{write} loops. (d) The normalized ρ_H (top) and J_{write} (bottom) for the Mn_3Sn device at room temperature for a series of applied positive and negative $J_{write} = 5 \times 10^6$ A·cm^{-2}, where ρ_H was measured at $I_{read} = 0.1$ mA after each writing current pulse. (e and f) ρ_H versus $\mu_0 H_Z$ and J_{write} loops for the Mn_3Sn device at room temperature. The minimum $\mu_0 H_Z^{min}$ and J_{write}^{min} determine the magnitude of the field- and current-driven Hall resistivity switching.

resistivity (Fig. 1e (top)). Moreover, the $M - \mu_0 H_Z$ curves were measured at different temperatures (T) using a vibrating sample magnetometer and the extracted magnetization of ~8 emu/cc at 300 K and 5 mT (Supplementary Fig. S5f), which is comparable with previous reported values [13,15,20,21]. The longitudinal resistivity and Hall resistivity as a function of temperature under zero magnetic field are illustrated in Supplementary Fig. S6. Both the $M - T$ and $\rho_H - T$ curves show a rapid decrease at ~250 K, which corresponds to the transition to spiral phase [22–24]. The Néel temperature T_N, corresponding to the disappearance of $\Delta\rho_H^0$ and $\mu_0 H_C$ of the anomalous Hall hysteresis loops, is found to be ~430 K (Fig. 1f and Supplementary Fig. S7), which is close to that of single crystal Mn_3Sn [9]. The results confirm that our thin films have physical properties similar to those of previous reports.

We then examined the possible current-induced topological non-collinear antiferromagnetic state switching. For the reference samples, the current-induced deterministic switching can only be observed under an auxiliary magnetic field for Ru/Mn_3Sn/Pt devices (Supplementary Fig. S8), which is consistent with previous works [13,14]. Interestingly, different current-induced switching behaviors were observed in our heavy-metal-layer-free devices. Figure 2a presents the $\rho_H - \mu_0 H_Z$ curve of a 50-nm-thick Mn_3Sn device. Under zero magnetic field, a 50-ms writing current pulse I_{write} followed by a DC reading current of $I_{read} = 0.1$ mA is applied along the x direction. Surprisingly, as shown by the black curve in Fig. 2b, the electrical current flowing through the device leads to a clear negative (positive) jump in ρ_H at a positive (negative) threshold writing current, implying a reversing of the z component of the octupole. The magnitude of the Hall resistivity jump $\Delta\rho_H^J$ is ~58% of $\Delta\rho_H^0$ in the field-swept measurements (Fig. 2a). Figure 2b also shows the $\rho_H - J_{write}$ loops in an in-plane magnetic field $\mu_0 H_x$ of ± 0.2 T and ± 0.4 T. With the increase of positive (negative) applied magnetic field, the gradual shift of $\rho_H - J_{write}$ loops toward a negative (positive) J_{write}, together with the reduction of $\Delta\rho_H^J$, is observed, which is clearer in the field dependence of the threshold current in Fig. 2c. The current-induced magnetization switching disappears for a sufficiently large bias field, e.g. 1 T $> \mu_0 H_C$, probably because the magnetic octupoles are aligned to the external field direction.

Compared with the Mn_3Sn/(heavy-) metal reference devices (Supplementary Fig. S8), here, the writing current is fully injected into the Mn_3Sn layer without passing through a highly conductive metal layer. In addition, the strong inversion asymmetry along the $x(y)$ direction was confirmed by our non-linear Hall measurements [25,26]. As a

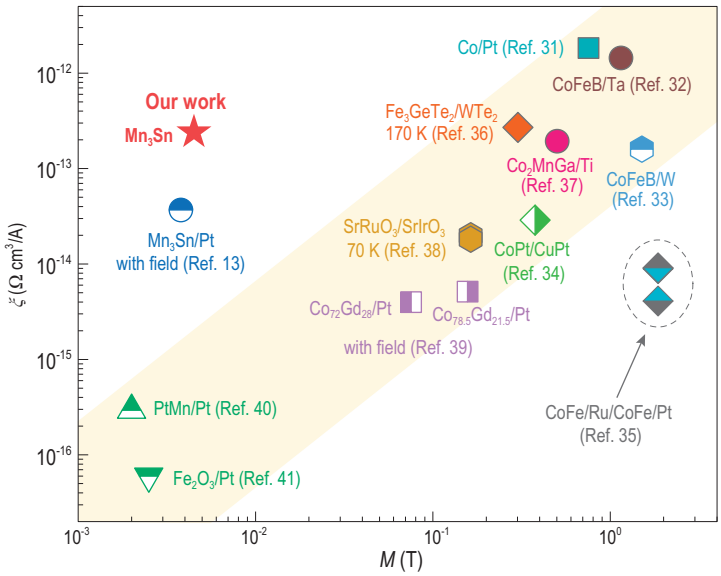

Figure 3. Readout efficiency as a function of magnetization. Double-logarithmic plot of the readout efficiency $\xi = \Delta\rho_H^J/J_c$ as a function of the magnetization M for various materials, including ferromagnets (Co/Pt [31], CoFeB/Ta [32], CoFeB/W [33], CoPt/CuPt [34], CoFe/Ru/CoFe/Pt [35], Fe_3GeTe_2/WTe_2 [36], Co_2MnGa/Ti [37] and $SrRuO_3/SrIrO_3$ [38]), ferrimagnets (Co_xGd_{1-x}/Pt [39]), collinear antiferromagnets (PtMn/Pt [40] and Fe_2O_3/Pt [41]) and Mn_3Sn/Pt [13], at various temperatures. The red star indicates our Mn_3Sn device at room temperature. The yellow shaded region highlights the scaling law of ξ with M.

low frequency AC current is applied along the $x(y)$ direction, a considerable second harmonic voltage is measured along the $y(x)$ direction in our Mn_3Sn device, probably due to the boundaries between grains and/or magnetic domains. The non-linear Hall effect in our Mn_3Sn device is considerably stronger than that measured in the reference samples, justifying a larger Rashba effect in the heavy-metal-layer-free device (Supplementary Fig. S9). We explain that the field-free deterministic switching originates from current-induced spin accumulations in the Mn_3Sn layer without inversion symmetry.

Notably, the critical writing current density J_c required for switching the octupole, at zero magnetic field, is estimated to be 5×10^6 A·cm^{-2} in our Mn_3Sn device, which is less than half that required for the reference Ru/Mn_3Sn/Pt/AlO_x sample. This is nearly one order of magnitude smaller than the recently reported value 4×10^7 A·cm^{-2} for the collinear antiferromagnet/Pt devices [4], and comparable to the values reported for antiferromagnet/ferromagnet [27] and collinear antiferromagnet devices [3,28]. The increase of the device temperature due to Joule heating at the maximum current pulse is estimated to be 38 K (Supplementary Fig. S10). The temperature of the device is still substantially lower than the Néel temperature (≈430 K) even when J_{write} is on, thus the Joule heating effect cannot be the predominant reason behind the observed switching. Furthermore, we performed the same zero-field current-induced switching measurements at lower temperatures (200 K and 250 K), which show similar behaviors of switching with slightly larger threshold currents (Supplementary Fig. S11).

Our experiments confirm that the deterministic switching of the Mn_3Sn devices is due to the current-induced torque exerted on the non-collinear antiferromagnetic spin texture. This reproducible bipolar switching can act as an antiferromagnetic memory. The alternating current pulses ($|J_{write}| > J_c$) along opposite directions switch the antiferromagnetic state back and forth reproducibly (Fig. 2d), indicating its reliable controllability. Remarkably, our Mn_3Sn device can provide multilevel signals by varying the magnitude of $\mu_0 H_Z$ or J_{write}. With a fixed maximum positive magnetic field (Fig. 2e) or writing current (Fig. 2f), the change of ρ_H increases with the increasing magnitude of $\mu_0 H_Z^{min}$ or J_{write}^{min} (Magnetic and magnetotransport measurements in Methods). This multilevel plasticity controlled by electrical currents at zero magnetic field suggests the great potential of Mn_3Sn in neuromorphic computing [21,27,29,30].

To compare the efficiency of the readout signal driven by an electrical current with that of other heavy-metal/magnet bilayer structures, we defined the readout efficiency as $\xi = \Delta\rho_H^J/J_c$. In the case of our Mn_3Sn device, ξ is ∼2.4×10^{-13} Ω·cm^3/A (marked with a red star in Fig. 3), which is close to readout efficiencies of ferromagnetic materials such as Co_2MnGa and CoFeB [31–38] but one to three orders of magnitude larger than those of ferrimagnets, collinear antiferromagnets and Mn_3Sn/Pt devices [13,39–41]. Interestingly, a scaling law of ξ with the magnetization M is observed for collinear antiferromagnets, ferrimagnets and ferromagnets, as indicated by the shaded region in Fig. 3. This is because the anomalous Hall resistance is proportional to the magnetization, whereas the critical switching current is insensitive to the magnetization in the case of the current-induced magnetization switching dominated by the spin Hall effect in heavy-metal/magnet bilayer systems [42]. The large ξ for Mn_3Sn is due to the strong anomalous Hall effect originating from the non-zero Berry curvature in momentum space [7,8]. The readout efficiency obtained in our pure Mn_3Sn is one order of magnitude higher than that in ref. [13], probably because our Mn_3Sn devices have higher inversion asymmetry and do not have a heavy-metal layer. We can thus achieve a strong readout anomalous Hall signal driven by a small writing current of 5×10^6 A·cm^{-2} in our Mn_3Sn device.

DISCUSSION

Now we illustrate the possible mechanisms of intrinsic non-collinear spin-orbit torques that induce the deterministic all-electrical switching in our Mn_3Sn device. We argue that the current-induced switching requires an inversion asymmetry in our polycrystal device, for the following reasons.

In our Mn_3Sn polycrystal, the measured nonzero anomalous Hall signal implies that the different configurations in our samples are not compensated. To understand this, we note that any crystal grain in the polycrystalline Mn_3Sn can be decomposed into the z–x, x–y and y–z configurations, according to the direction of kagome plane (Fig. 4a). The octupole rotates only in the kagome plane, so the out-of-plane magnetic field H_z can only switch configurations z–x and y–z. Considering the weak tunneling between the kagome layers, I_x is not expected to be able to switch configuration y–z effectively, i.e. the in-plane current I_x can only switch configurations z–x and x–y. The anomalous Hall signal depends on the z component of the octupole, so V_{AHE} can be used to read out only configurations z–x and y–z. This infers that the Hall response of the $\mu_0 H_z$-hysteresis is around 2 to 2.3 times (considering that the octupole may relax at positions within ± 30 degrees from the full polarization) that of the J_{write}-hysteresis, close to the data in Fig. 2a and b. According to the above discussion, only configuration z–x in Fig. 4a can be switched by the current and is measurable by the anomalous Hall effect.

More importantly, the z–x configuration of single-crystal Mn_3Sn requires an inversion asymmetry to be deterministically switched. Because the octupole is a pseudo vector, which is invariant under inversion, it does not reverse as the current changes sign, if there is inversion symmetry (see also the symmetry and microscopic analysis in Supplementary Sections S13 and S14). The occurrence of the inversion asymmetry in polycrystalline Mn_3Sn was confirmed by our non-linear Hall measurements. The inversion asymmetry can induce Rashba-like spin-orbit coupling, which can convert the injected electric current into spin currents or spin accumulations. The spin accumulations, when not aligned with the local Mn moments, can induce intrinsic non-collinear spin-orbit torques to rotate the Mn moments. The octupole is defined by the Mn moments in the Mn_3Sn magnetic structure with inverse triangular spin structure (Supplementary Sections S15). Thus, in this sense, it is switchable by the current, and its z component leads to a measurable anomalous Hall signal.

To verify our speculations regarding the microscopic mechanism behind the observed switching, we performed numerical simulations for the octupole polarization. For a given electrical current I_x, the simulation starts with an initial magnetic structure of the Mn moments $\mathbf{m}_{ia}$, which behave as local Zeeman fields on the electrons described by an s–d model. Using the linear-response theory, the local spin accumulations induced by the current in the presence of the Rashba spin-orbit coupling are calculated. The effective magnetic field of the spin accumulations is then converted into magnetic torques $\mathbf{T}_{ia}$ in the Landau-Lifshitz-Gilbert equation to generate a new magnetic structure. The above steps are iterated until the magnetic structure converges to yield the octupole moment for the given injected current (see details in Methods Section simulating current-induced switching of the non-collinear antiferromagnet).

Figure 4b shows the simulated octuple angle φ as a function of time at different current intensities, which demonstrates that the current must be sufficiently strong to drive a switching. Its insets also show the microscopic dynamics in terms of the calculated torques being exerted on the Mn moments at different stages of a successful switching for I_x, well above the critical value. The non-collinear antiferromagnetic structure tends to be maintained during the switching, and the rotation of the Mn moments (collectively as octupole) is determined by the sum of the nutation tendencies of the sublattice moments driven by the torques. Figure 4c–e shows that a larger Rashba spin-orbit coupling λ_R leads to an enhanced spin accumulation, faster switching and a smaller critical current. Figure 4f shows that increasing/decreasing the magnetic-structure parameters $K/(J_m, D)$ leads to a failed/faster switching, where J_m and D stabilize the inverse 120° triangular structure, whereas K introduces a small deviation to exert torques that relax the octupole to one of the six stable positions ($\varphi = \pi/6+$ integer times of $\pi/3$). In other words, the switching requires the torques from the current-induced spin accumulations to overcome the stable-position-favored torques due to the magnetic structure, which favors the six stable positions. Figure 4g shows that the hysteresis loop can be shifted by the x-direction magnetic field of ± 0.0012 T (the theoretical values are usually magnitudes smaller than those in the experiments [9,13], probably because the external magnetic field is screened in the realistic polycrystals). More importantly, the simulations confirm that, without external magnetic fields and heavy metals, the all-electrical switching of the non-collinear antiferromagnet can be achieved, owing to the intrinsic non-collinear spin-orbit torques from the current-induced local spin accumulations in Mn_3Sn itself.

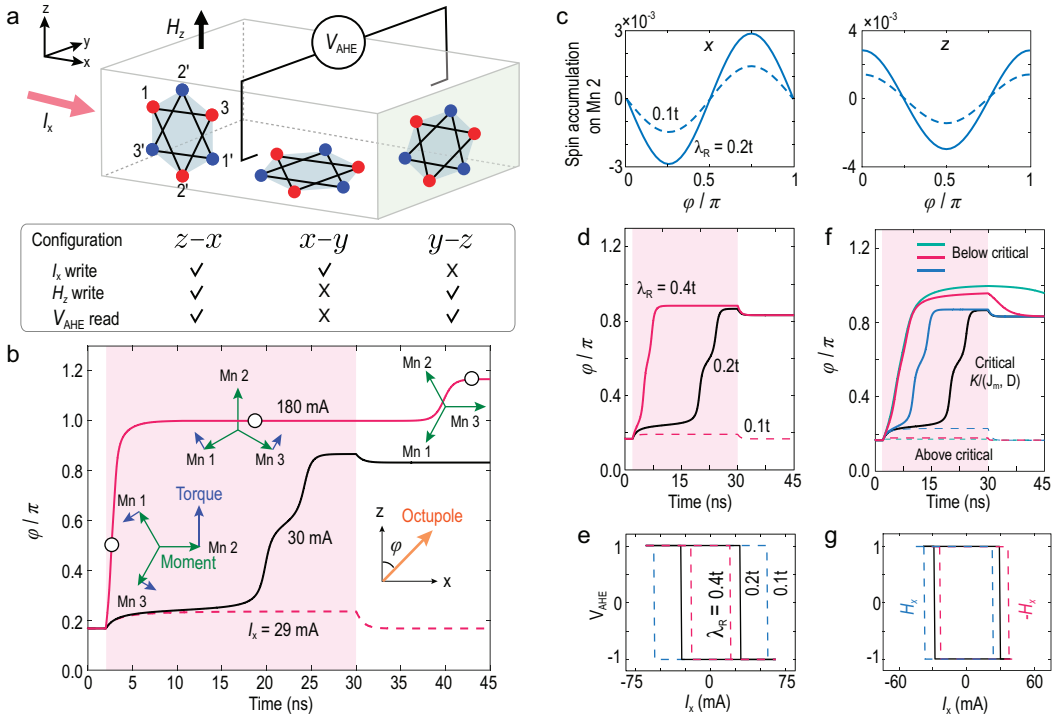

Figure 4. Numerically simulated switching of the Mn_3Sn octupole. The spin-orbit coupling converts the current I_x (experimental J_{write}) into spin accumulations, which exert intrinsic non-collinear spin-orbit torques to rotate the Mn moments and octupole. (a) The kagome lattices in polycrystal can be decomposed into three configurations, z–x, x–y and y–z. I_x can switch configurations z–x and x–y and V_{AHE} can read out configurations z–x and y–z, so the simulation focuses on configuration z–x. (b) Simulated octupole angle φ versus time, driven by a I_x pulse with duration of 2–30 ns (pink shadowed region), for I_x below (29 mA), at (30 mA), and well above (180 mA) the critical current. For I_x= 180 mA, the insets show the dynamics of the torques (blue arrows) being exerted on the Mn moments (green arrows), at three stages (hollow circles), as φ starts from $\pi/6$ (an easy axis), then is switched to π (normal to I_x) after turning on I_x, and finally relaxes to $7\pi/6$ (another easy axis) after turning off I_x. (c) Simulated x- and z-direction spin accumulations on Mn 2 (denoted in panel (a)) as a function of φ, for different Rashba spin-orbit coupling λ_R (Equation 2 in Methods of Supplementary). (d) The same as the 30 mA case in panel (b), but also for λ_R below and above the critical value. (e) Simulated hysteresis loops of the Hall response V_{AHE} driven by I_x, for different λ_R. (f) The same as the 30 mA case in panel (b). Combinations of the magnetic-structure parameters $K/(J_m, D)$ (Equation 1 in Methods of Supplementar) below (solid curves) and above (dashed curves) the critical combination are also considered. (g) The same as the $\lambda_R = 0.2t$ case in panel (e). The presence of the x-axis magnetic field H_x is also considered. More simulation results by changing λ_R, $K/(J_m, D)$, and initial states can be found in Supplementary Section S16.

CONCLUSIONS

Our findings promise potential applications of Mn_3Sn in information technologies. Specifically, the all-electrical control of the binary and multilevel states with large Mn_3Sn readout signals could act as the building block for magnetic random-access memory and artificial synapses, respectively. Furthermore, in-memory computing may also be achieved by utilizing the all-electrical control of topological non-collinear antiferromagnets.

METHODS

Sample and device fabrication

The samples used for the current-induced switching measurements, which consist of Mn_3Sn (50)/AlO_x (2) (the thicknesses shown in parentheses are in nanometers), were grown on thermally oxidized Si substrates. The top AlO_x layer was used as the capping layer. For comparison, reference samples consisting of Ru (3)/Mn_3Sn (50)/AlO_x (2) and Ru (3)/Mn_3Sn (50)/Pt (8)/AlO_x (2) were also deposited on Si/SiO_2. The Mn_3Sn, Ru and Pt layers were deposited at room temperature using a DC magnetron sputtering system with a base pressure of $<5 \times 10^{-9}$ Torr (at rates of ∼0.05, 0.01 and 0.02 nm/s, power of 30 W and Ar gas pressure of 0.8 mTorr). Next, the AlO_x layers were grown using an radio frequency (RF) magnetron sputtering system with a power of 80 W and Ar gas pressure of 2 mTorr. The Mn_3Sn (50)/AlO_x (2), Ru (3)/Mn_3Sn (50)/AlO_x (2) and Ru (3)/Mn_3Sn (50)/Pt (8)/AlO_x (2) samples were then annealed

at 450°C for 1 hour using a vacuum annealing furnace (F800-35, East Changing Technologies, China) at a base pressure of 5×10^{-7} Torr. The samples were patterned into Hall bar devices with a current channel width of 10 μm using standard photolithography and Ar-ion etching. For more methods of measurement and simulation, see the Methods section in the supplementary materials.

ACKNOWLEDGEMENTS

The authors thank Prof. Hong Ding for fruitful discussions.

FUNDING

This work was supported by the National Key R&D Program of China (2017YFA0303400), the National Natural Science Foundation of China (11474272 and 11925402), the Chinese Academy of Sciences (QYZDY-SSW-JSC020, XDB28000000 and XDB44000000), the Beijing Natural Science Foundation (2212048), the Beijing Natural Science Foundation Key Program (Z190007), Guangdong (2016ZT06D348 and 2020KCXTD001), Shenzhen (G02206304, G02206404, ZDSYS20170303165926217 and JCYJ20170412152620376) and the Center for Computational Science and Engineering of SUSTech.

AUTHOR CONTRIBUTIONS

K.W. conceived the work. Y.D. and X.L. grew the films, fabricated the devices and carried out the electrical transport measurements. N.J. and C.S. measured the magnetic properties of the samples. Y.D., X.L. and K.W. analyzed the data. Y.C., Z.D. and H.L. performed theoretical calculations. Y.D., X.L., H.L. and K.W. wrote the manuscript. All the authors discussed the results and commented on the manuscript.

Conflict of interest statement. None declared.

REFERENCES

1. Železný J, Wadley P and Olejník K *et al.* Spin transport and spin torque in antiferromagnetic devices. *Nat Phys* 2018; **14**: 220–8.
2. Manchon A, Železný J and Miron IM *et al.* Current-induced spin-orbit torques in ferromagnetic and antiferromagnetic systems. *Rev Mod Phys* 2019; **91**: 035004.
3. Wadley P, Howells B and Elezny J *et al.* Electrical switching of an antiferromagnet. *Science* 2016; **351**: 587–90.
4. Chen XZ, Zarzuela R and Zhang J *et al.* Antidamping-torque-induced switching in biaxial antiferromagnetic insulators. *Phys Rev Lett* 2018; **120**: 207204.
5. Šmejkal L, Mokrousov Y and Yan B *et al.* Topological antiferromagnetic spintronics. *Nat Phys* 2018; **14**: 242–51.
6. Zhang Y, Sun Y and Yang H *et al.* Strong anisotropic anomalous Hall effect and spin Hall effect in the chiral antiferromagnetic compounds Mn_3X (X = Ge, Sn, Ga, Ir, Rh, and Pt). *Phys Rev B* 2017; **95**: 075128.
7. Yang H, Sun Y and Zhang Y *et al.* Topological Weyl semimetals in the chiral antiferromagnetic materials Mn_3Ge and Mn_3Sn. *New J Phys* 2017; **19**: 015008.
8. Kuroda K, Tomita T and Suzuki M-T *et al.* Evidence for magnetic Weyl fermions in a correlated metal. *Nat Mater* 2017; **16**: 1090–5.
9. Nakatsuji S, Kiyohara N and Higo T. Large anomalous Hall effect in a non-collinear antiferromagnet at room temperature. *Nature* 2015; **527**: 212–5.
10. Ikhlas M, Tomita T and Koretsune T *et al.* Large anomalous Nernst effect at room temperature in a chiral antiferromagnet. *Nat Phys* 2017; **13**: 1085–90.
11. Železný J, Zhang Y and Felser C *et al.* Spin-polarized current in noncollinear antiferromagnets. *Phys Rev Lett* 2017; **119**: 187204.
12. Suzuki MT, Koretsune T and Ochi M *et al.* Cluster multipole theory for anomalous Hall effect in antiferromagnets. *Phys Rev B* 2017; **95**: 094406.
13. Tsai H, Higo T and Kondou K *et al.* Electrical manipulation of a topological antiferromagnetic state. *Nature* 2020; **580**: 608–13.
14. Takeuchi Y, Yamane Y and Yoon J-Y *et al.* Chiral-spin rotation of non-collinear antiferromagnet by spin–orbit torque. *Nat Mater* 2021; **20**: 1364–70.
15. Higo T, Qu D and Li Y *et al.* Anomalous Hall effect in thin films of the Weyl antiferromagnet Mn_3Sn. *Appl Phys Lett* 2018; **113**: 202402.
16. Matsuda T, Kanda N and Higo T *et al.* Room-temperature terahertz anomalous Hall effect in Weyl antiferromagnet Mn_3Sn thin films. *Nat Commun* 2020; **11**: 909.
17. Markou A, Taylor JM and Kalache A *et al.* Noncollinear antiferromagnetic Mn_3Sn films. *Phys Rev Mater* 2018; **2**: 051001.
18. Nakano T, Higo T and Kobayashi A *et al.* Fabrication of polycrystalline Weyl antiferromagnetic Mn_3Sn thin films on various seed layers. *Phys Rev Mater* 2021; **5**: 054402.
19. Nandy S, Sharma G and Taraphder A *et al.* Chiral anomaly as the origin of the planar Hall effect in Weyl semimetals. *Phys Rev Lett* 2017; **119**: 176804.
20. Taylor JM, Markou A and Lesne E *et al.* Anomalous and topological Hall effects in epitaxial thin films of the noncollinear antiferromagnet Mn_3Sn. *Phys Rev B* 2020; **101**: 094404.
21. Higo T, Li Y and Kondou K *et al.* Omnidirectional control of large electrical output in a topological antiferromagnet. *Adv Funct Mater* 2021; **31**: 2008971.
22. Ohmori H, Tomiyoshi S and Yamauchi H *et al.* Spin structure and weak ferromagnetism of Mn_3Sn. *J Magn Magn Mater* 1987; **70**: 249–51.
23. Brown PJ, Nunez V and Tasset F *et al.* Determination of the magnetic structure of Mn_3Sn using generalized neutron polarization analysis. *J Phys: Condens Matter* 1990; **2**: 9409–22.
24. Sung NH, Ronning F and Thompson JD *et al.* Magnetic phase dependence of the anomalous Hall effect in Mn_3Sn single crystals. *Appl Phys Lett* 2018; **112**: 132406.
25. Ma Q, Xu S-Y and Shen H *et al.* Observation of the nonlinear Hall effect under time-reversal-symmetric conditions. *Nature* 2019; **565**: 337–42.

26. Du ZZ, Lu H-Z and Xie XC. Nonlinear Hall effects. *Nat Rev Phys* 2021; **3**: 744–52.
27. Fukami S, Zhang C and DuttaGupta S *et al.* Magnetization switching by spin–orbit torque in an antiferromagnet–ferromagnet bilayer system. *Nat Mater* 2016; **15**: 535–41.
28. Bodnar SY, Šmejkal L and Turek I *et al.* Writing and reading antiferromagnetic Mn_2Au by Néel spin-orbit torques and large anisotropic magnetoresistance. *Nat Commun* 2018; **9**: 348.
29. Cao Y, Rushforth AW and Sheng Y *et al.* Tuning a binary ferromagnet into a multistate synapse with spin–orbit-torque-induced plasticity. *Adv Funct Mater* 2019; **29**: 1808104.
30. Hajiri T, Matsuura K and Sonoda K *et al.* Spin-orbit-torque switching of non-collinear antiferromagnetic antiperovskite manganese nitride Mn_3GaN. *Phys Rev Appl* 2021; **16**: 024003.
31. Yang M, Luo J and Ji Y *et al.* Spin logic devices via electric field controlled magnetization reversal by spin-orbit torque. *IEEE Electron Device Lett* 2019; **40**: 1554–7.
32. Yu G, Upadhyaya P and Fan Y *et al.* Switching of perpendicular magnetization by spin–orbit torques in the absence of external magnetic fields. *Nat Nanotechnol* 2014; **9**: 548–54.
33. Murray N, Liao W-B and Wang T-C *et al.* Field-free spin-orbit torque switching through domain wall motion. *Phys Rev B* 2019; **100**: 104441.
34. Liu L, Zhou C and Shu X *et al.* Symmetry-dependent field-free switching of perpendicular magnetization. *Nat Nanotechnol* 2021; **16**: 277–82.
35. Lau Y-C, Betto D and Rode K *et al.* Spin–orbit torque switching without an external field using interlayer exchange coupling. *Nat Nanotechnol* 2016; **11**: 758–62.
36. Shin I, Cho WJ and An E *et al.* Spin–orbit torque switching in an all-Van der Waals heterostructure. *Adv Mater* 2022; **34**: 2101730.
37. Tang K, Wen Z and Lau YC *et al.* Magnetization switching induced by spin-orbit torque from Co_2MnGa magnetic Weyl semimetal thin films. *Appl Phys Lett* 2021; **118**: 062402.
38. Liu L, Qin Q and Lin W *et al.* Current-induced magnetization switching in all-oxide heterostructures. *Nat Nanotechnol* 2019; **14**: 939–44.
39. Mishra R, Yu J and Qiu X *et al.* Anomalous current-induced spin torques in ferrimagnets near compensation. *Phys Rev Lett* 2017; **118**: 167201.
40. DuttaGupta S, Kurenkov A and Tretiakov OA *et al.* Spin-orbit torque switching of an antiferromagnetic metallic heterostructure. *Nat Commun* 2020; **11**: 5715.
41. Cheng Y, Yu S and Zhu M *et al.* Electrical switching of tristate antiferromagnetic Néel order in α-Fe_2O_3 epitaxial films. *Phys Rev Lett* 2020; **124**: 027202.
42. Liu L, Lee OJ and Gudmundsen TJ *et al.* Current-induced switching of perpendicularly magnetized magnetic layers using spin torque from the spin Hall effect. *Phys Rev Lett* 2012; **109**: 096602.